Sensitivity comparison of absorption and grating-based phase tomography of paraffin-embedded human brain tissue

Christos Bikis [iD], Griffin Rodgers [iD], Hans Deyhle, Peter Thalmann, Alexander Hipp [iD], Felix Beckmann [iD], Timm Weitkamp [iD], Stamatios Theocharis [iD], Christoph Rau, Georg Schulz [iD], and Bert Müller [iD]

View Online   Export Citation   CrossMark

ARTICLES YOU MAY BE INTERESTED IN

Understanding the charge transport mechanisms through ultrathin SiO_X layers in passivated contacts for high-efficiency silicon solar cells
Applied Physics Letters **114**, 083902 (2019); https://doi.org/10.1063/1.5081832

3-D underwater acoustic wave focusing by periodic structure
Applied Physics Letters **114**, 081908 (2019); https://doi.org/10.1063/1.5081661

Thermally tunable asymmetric metamolecule
Applied Physics Letters **114**, 082901 (2019); https://doi.org/10.1063/1.5061720

2017 Journal
Impact Factor:
12.894

Applied Physics Reviews
Now accepting original research

Sensitivity comparison of absorption and grating-based phase tomography of paraffin-embedded human brain tissue

Christos Bikis,[1] [iD] Griffin Rodgers,[1,a)] [iD] Hans Deyhle,[1] Peter Thalmann,[1] Alexander Hipp,[2] [iD] Felix Beckmann,[2] [iD] Timm Weitkamp,[3] [iD] Stamatios Theocharis,[4] [iD] Christoph Rau,[5] Georg Schulz,[1] [iD] and Bert Müller[1] [iD]

AFFILIATIONS

[1]Biomaterials Science Center, University of Basel, 4123 Allschwil, Switzerland
[2]Institute of Materials Research, Helmholtz-Zentrum Geesthacht, 21502 Geesthacht, Germany
[3]Synchrotron Soleil, 91192 Gif-sur-Yvette, France
[4]National and Kapodistrian University of Athens, 11527 Athens, Greece
[5]Diamond Light Source Ltd., Didcot OX11 0DE, United Kingdom

[a)]Electronic mail: griffin.rodgers@unibas.ch

ABSTRACT

Advances in high-resolution hard X-ray computed tomography have led to the field of virtual histology to complement histopathological analyses. Phase-contrast modalities have been favored because, for soft tissues, the real part of the refractive index is orders of magnitude greater than the imaginary part. Nevertheless, absorption-contrast measurements of paraffin-embedded tissues have provided exceptionally high contrast combined with a submicron resolution. In this work, we present a quantitative comparison of phase tomography using synchrotron radiation-based X-ray double grating interferometry and conventional synchrotron radiation-based computed tomography in the context of histopathologically relevant paraffin-embedded human brain tissue. We determine the complex refractive index and compare the contrast-to-noise ratio (CNR) of each modality, accounting for the spatial resolution and optimizing the photon energy for absorption tomography. We demonstrate that the CNR in the phase modality is 1.6 times higher than the photon-energy optimized and spatial resolution-matched absorption measurements. We predict, however, that a further optimized phase tomography will provide a CNR gain of 4. This study seeks to boost the discussion of the relative merits of phase and absorption modalities in the context of paraffin-embedded tissues for virtual histology, highlighting the importance of optimization procedures for the two complementary modes and the trade-off between spatial and density resolution, not to mention the disparity in data acquisition and processing.

Since the invention of the Bonse-Hart interferometer,[1] X-ray phase contrast imaging has been preferentially considered for light elements, i.e., the main constituents of human tissues, for which the decrement of the real part of the refractive index δ is three orders of magnitude larger than the imaginary part β at photon energies on the order of 10 keV.[2] Therefore, researchers estimated that phase-contrast tomography could reach a hundred to thousand times greater sensitivity than absorption-contrast tomography.[3,4] Pioneering tomography studies with hard X-rays revealed that not only the widely used absorption-contrast and the newer phase-contrast imaging techniques provide complementary information but also phase imaging yields a substantially better contrast-to-noise ratio (CNR) than absorption. During the last two decades, high-resolution tomography in the phase-contrast mode has enabled the visualization of individual cells[5] and even sub-cellular details[6,7] in the *post mortem* human brain. High-resolution X-ray phase-contrast tomography shows great promise for augmenting standard pathology in research and clinics with the so-called virtual histology.[8–10]

Several experimental results, however, indicate that conventional X-ray absorption tomography provides comparable CNR to phase tomography for paraffin-embedded soft tissues, i.e., those used in typical histopathological analysis. For example, conventional tomography of the paraffin-embedded brain[11] and peripheral nerves[12] has yielded sufficient CNR to identify biological cells and related microstructures. Thus, it is still unclear which method is more effective for the visualization of anatomical features in human tissues in the context of virtual histology.

Consequently, the aim of the present tomography study is a quantitative comparison of the density resolution of absorption- and phase-contrast modalities in the case of histopathologically relevant biological specimens embedded in paraffin. To this end, part of a formalin-fixated and paraffin-embedded human cerebellum was three-dimensionally visualized by means of conventional synchrotron radiation-based microcomputed tomography (SRμCT) and double-grating interferometry (XDGI). For a complete comparison, SRμCT data were also recorded at an optimized photon energy significantly lower for the chosen sample than the energy used for XDGI. The tomography datasets were rigidly registered, and the common volume was extracted to generate bivariate distributions to directly compare the CNR. Additionally, the absorption projections were filtered to compare the CNR of the modalities at an equal spatial resolution.

The human cerebellum specimen was selected with informed consent for scientific use. All the associated procedures were conducted in accordance with the Declaration of Helsinki and were approved by the ethics committee of the Medical School of the National and Kapodistrian University of Athens. The brain was extracted *post mortem* from a donated body and fixed in 4% histological-grade buffered paraformaldehyde. To allow for sufficient perfusion of solvents and liquid paraffin, 2-cm-thick cerebellum slices were produced, dehydrated in ascending ethanol solutions, transferred to xylene, and finally embedded in a paraffin/plastic polymer mixture, following the standard pathology procedure. Out of the obtained paraffin blocks, cylinders 6 mm in diameter were obtained by means of a stainless-steel punch.

The wavefront ψ immediately after passing through the specimen is given by projection approximation[13]

$$\psi(x,y,z) = \psi(x,y,0)\exp\left[-ik\int_0^z[\delta(x,y,z) - i\beta(x,y,z)]dz\right],$$

where k is the wavenumber and z the propagation direction. A detector placed near the sample measures the modulus squared of the wavefront, accessing the imaginary part of the index of refraction

$$I(x,y) = I_0(x,y)\exp\left[-2k\int\beta(x,y,z)dz\right].$$

This expression is equivalent to Beer's law, with the linear attenuation coefficient $\mu = 2k\beta$. If a grating interferometer is placed behind the sample, the interference pattern fringes are shifted laterally by an angle α_x given by the derivative of the wavefront phase shift

$$\alpha_x(x,y) = \frac{\partial\phi(x,y)}{\partial x} = \frac{\partial}{\partial x}\int\delta(x,y,z)dz.$$

Phase stepping allows for retrieval of α_x, and reconstruction with a modified filter kernel allows for δ-retrieval.[14,15]

Phase and absorption tomography measurements using a photon energy of 20 keV, denoted DPC 20 and ABS 20, were performed at the Diamond Manchester Imaging Beamline [I13-2, Diamond Light Source (DLS), UK]. Additionally, an absorption tomography measurement at a photon energy of 10 keV, denoted ABS 10, was performed at the P05 beamline (PETRA III, DESY, Hamburg, Germany), a facility operated by the Helmholtz-Zentrum Geesthacht.

This study comprises at least seven parameters. The impact of these parameters has been considered, allowing for a comparison of

the three dominant factors: (i) the contrast mechanisms, (ii) the selection of photon energy for absorption, and (iii) the balancing of the spatial resolution.

For a homogeneous specimen of diameter D with a linear attenuation coefficient $\mu(E)$, the optimal photon energy for an absorption measurement is found by setting $\mu(E) \times D = 2$.[16] For inhomogenous specimens, a lower value is usually chosen. This value was 0.3 and 1.6 for ABS 20 and ABS 10, respectively, indicating that 10 keV is closer to the optimum efficiency criteria.

The XDGI setup consisted of a beam-splitting absorption grating and an equivalent analyzer grating with a periodicity of $p_1 = p_2 = 7\,\mu$m and a gold structure height of $70\,\mu$m. The ideal transmission of this interferometer is 25%. An inter-grating distance of 80 cm was used, corresponding to the first fractional Talbot order. Five phase step images were recorded per projection. The setup had a mean visibility of 35%.

Between DPC 20 and ABS 20, the gratings and the water bath (used to avoid phase wrapping) were removed, the exposure time reduced, and the detector distance set to 7 cm. This was the minimum distance without changing the rotation stage. For ABS 10, the specimen-detector distance was 1 cm to reduce edge enhancement. All projections were 2×2 binned to improve the signal and ease data handling.[17] Table I lists the acquisition parameters.

The phase retrieval for DPC 20 was performed by applying a pixel-wise Fourier analysis.[14] The tomographic reconstruction relied on the standard filtered back-projection algorithm, which is implemented in Matlab (The MathWorks, Inc., Natick, USA), using a modified filter kernel (Hilbert transform).[15] Prior to reconstruction, Gaussian filters with $\sigma = 1.52$ and $\sigma = 1.48$ pixels were applied to the projections of ABS 20 and ABS 10, respectively. This filter size matched p_2, which is the lower resolution limit of the phase measurement.[14] The approximately equal spatial resolution was confirmed by

TABLE I. Acquisition parameters for the three measurements. Effective pixel sizes contain the magnification and binning.

	DPC 20	ABS 20	ABS 10
Facility	DLS	DLS	DESY
Photon energy	20 keV	20 keV	10 keV
Camera	pco.4000[a]	pco.4000[a]	KAF-09000[b]
Array (binned)	2004×1336	2004×1336	1528×1528
Scintillator	LuAG	LuAG	CdWO$_4$
	$500\,\mu$m	$500\,\mu$m	$100\,\mu$m
Objective	PLAPON 2×[c]	PLAPON 2×[c]	POG 5×[d]
Numerical aperture	0.08	0.08	0.25
Effective pixel size	$4.6\,\mu$m	$4.6\,\mu$m	$4.8\,\mu$m
Detector distance	80 cm	7 cm	1 cm
t_{exp}	5×5 s	2 s	1.5 s
# counts	5×2500	10 000	32 000
# projections	1201	1201	1201
Medium	Water	Air	Air

[a]PCO AG, Kelheim, Germany.
[b]EHD SciCam, EHD Imaging GmbH, Damme, Germany.
[c]Olympus Corporation, Tokyo, Japan.
[d]Präzisionsoptik Gera GmbH, Löbichau, Germany.

the selected line profiles, where the number of pixels defining the edges between paraffin and the molecular layer for the filtered absorption-contrast datasets was less than or equal to that for the phase-contrast dataset.

To obtain meaningful bivariate histograms, also known as joint histograms, the data have to be precisely registered. Therefore, an affine three-dimensional registration was performed by means of an algorithm to maximize mutual information,[18–20] with ABS 20 selected as a reference and DPC 20 or ABS 10 as the floating dataset. Tricubic interpolation was used for visualization, while the nearest neighbor interpolation was used for the analysis in order to avoid smoothing of the floating datasets.

Figure 1 shows a slice through the registered reconstructions of (a) DPC 20, (b) filtered and (c) unfiltered ABS 10, and (d) filtered and (e) unfiltered ABS 20. Related zoom-in views are given on the right to better visualize the (anatomical) features, i.e., the paraffin (PA), the molecular layer (ML), and the granular layer (GL). Purkinje cells can be identified between the ML and GL, see, e.g., bright dots in the zoomed view of (b). The white matter (WM) is found on the right side of each slice, with grayscale values between ML and GL.

Joint histograms from common volumes of tomography datasets allow for segmentation of specimen components[21,22] and direct comparison of the density resolution. Figure 2 shows the joint histograms of DPC 20 and filtered ABS 10 and filtered ABS 20. The histograms fit with a four-Gaussian model were chosen to match the number of features. The center and the width of the Gaussians are superimposed onto the joint histogram as a visual aid. The superior CNR of DPC 20 compared to the filtered ABS 20 is clear from the broadening of the Gaussian peaks. This is less evident for DPC 20 compared to ABS 10.

Equally sized regions of interest were selected within homogeneous areas characteristic of each (anatomical) feature in order to determine their index of refraction and the CNR. Paraffin was used as the reference material, as the surrounding medium was water for DPC 20 and air for ABS 20 and ABS 10. The measured $\Delta\delta \pm \sigma_\delta$ (or $\Delta\beta \pm \sigma_\beta$) values and the mean CNRs are shown in Table II. Both the histogram fits from Fig. 2 and the values from Table II indicate a nearly linear relationship between the real and imaginary parts of the refractive index, with $\Delta\delta/\Delta\beta \approx 700$ at 20 keV.

We define the Relative Contrast Gain (RCG) as the ratio of the CNR of the phase dataset over various absorption datasets.[23–25] The filtered datasets have a similar spatial resolution, and therefore, the RCG indicates the image quality improvement of phase contrast compared to absorption contrast. The RCG depends not only on $\Delta\delta/\Delta\beta$ but also on the sensitivity of the grating interferometer and on the tomographic reconstruction.

Table II shows the CNR and RCG for each dataset. Higher RCG values indicate a larger advantage of phase contrast over the dataset in question. Filtering increased the CNR by a factor of around 14 (5) for ABS 20 (ABS 10), underlining the importance of a comparison at an equal spatial resolution. The current study should initiate a detailed experimental study to understand the improvement of tomographic data quality by Gaussian filtering.

The absorption datasets, particularly ABS 20, where the sample-detector distance was larger, show edge enhancement, and thus, the phase retrieval proposed by Paganin et al. was applied.[26] Like Gaussian filtering, this reduces the noise at the expense of spatial resolution. The phase-retrieved 20 keV absorption dataset with δ/β of 100,
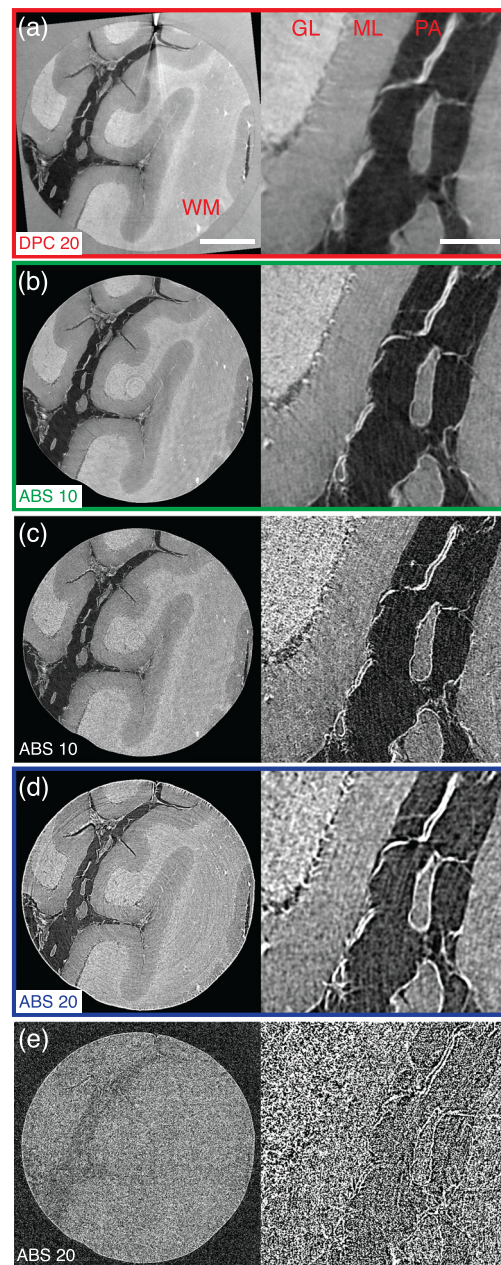

FIG. 1. One slice of the registered reconstructions of (a) DPC 20, (b) filtered (σ = 1.48 pixels) and (c) unfiltered ABS 10, and (d) filtered (σ = 1.52 pixels) and (e) unfiltered ABS 20. Features are indicated in (a): paraffin (PA), molecular layer (ML), granular layer (GL), and white matter (WM). Zoom-in views show a similar spatial resolution for (a)–(d). Gaussian filtering significantly improved CNR [(c) vs. (b) and (e) vs. (d)]. The scale bar in the slice (zoom) corresponds to 1.5 mm (150 μm). The gray scale corresponds to (a) $\Delta\delta = [-1.1, 6.5] \times 10^{-8}$, (b) and (c) $\Delta\beta = [-1.4, 6.6] \times 10^{-10}$, and (d) and (e) $\Delta\beta = [-0.4, 1.1] \times 10^{-10}$.

200, 500, and 1000 had CNR of 2.48, 4.16, 8.45, and 14.24, respectively. The spatial resolution of δ/β of 200–500 matched the grating-based phase and filtered absorption datasets, based on the spectral power. Thus, in the context of the 20 keV measurement, Gaussian filtering
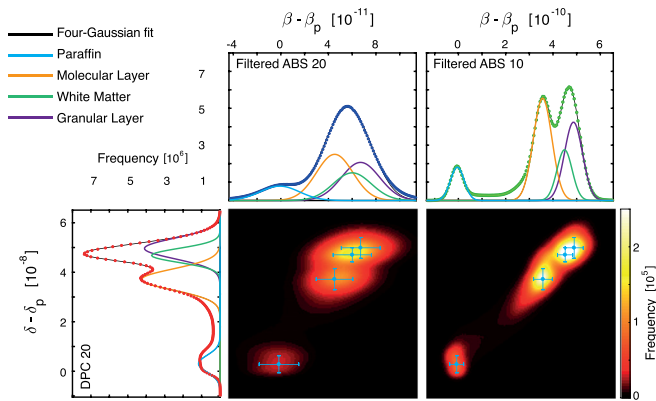
FIG. 2. Joint histograms of the filtered ABS 20 (middle) and filtered ABS 10 (right) with the DPC 20 dataset (y-axis). Individual histograms are also shown, which correspond to the projection of the joint histograms. Multi-Gaussian fits of the histograms are shown, with four Gaussians equal to the number of anatomical features. The centers and widths of these Gaussian fits are plotted on the joint histograms as a visual aid. The filtered ABS 20 has the lowest CNR, as evidenced by the broadest peaks. DPC 20 and the filtered ABS 10 show similar CNR. The peaks in the joint histograms indicate an approximately linear relationship between the real and complex parts of the refractive index throughout the specimen.

and Paganin's method produced similar image quality although the sample-detector distance was not optimized for Paganin's method.[26] The Gaussian filter was selected for this study because it requires no *a priori* knowledge of the refractive index and, unlike, e.g., binning, allows for fine control of the kernel size in order to match the spatial resolution between the datasets.

Photon energy optimization plays a large role in reducing the RCG (or increasing CNR) for the absorption measurements. $\Delta\beta$ increased by a factor of over 7 by decreasing the photon energy from 20 keV to 10 keV, creating a larger difference in absorption, while still allowing sufficient transmission for counting statistics. Adjusting the photon energy greatly impacts the count rate due to the details of the insertion device, optics, and the detection system at each synchrotron facility. In our case, the count rate is more than tripled for the measurement at lower photon energy. Together, the higher count rate and the lower energy provided a CNR improvement of around 7 (2.5) for the unfiltered (filtered) datasets. Typically, photon energy is not optimized in XDGI measurements because gratings are designed for operation at a few specific energies.

For larger specimens, the criteria proposed by Grodzins suggest a higher optimal energy.[16] For example, an entire rat brain (assuming a diameter of 12.5 mm) has an optimal photon energy of around 15 keV, while for a human brain (diameter 100 mm), it is around 50 keV. Therefore, it is not always the case that taking absorption at lower energies than the phase will improve the CNR. Nevertheless, most grating interferometers are designed for one specific energy, which may not be close to the optimal energy for absorption or phase measurements of a given specimen. The optimization of photon energy for grating-based phase contrast has not been experimentally studied. This study focuses on the case of 6 mm punches, a typical size for high resolution computed tomography experiments with effective pixel sizes in the micrometer range and fields-of-view of several millimeters.

The sensitivity of a grating interferometer can be described by the minimum resolvable deflection angle[27]

$$\alpha_{min} = \frac{p_2}{2\pi d} \frac{2}{V\sqrt{N}}.$$

Thus, the effect of increased counts can be extrapolated by the $\sqrt{N}$ term, with the caveat that low count rates may lead to reduced visibility or a degraded spatial resolution due to mechanical instabilities over longer acquisition times. The relationship between the period of the second grating p_2, the inter-grating distance d, and the visibility V is more complex. The visibility depends on the transverse coherence length, $l_c = \lambda L/s$ (photon wavelength λ, source-sample distance L, and source size s), p_2, and the Talbot order n[28]

$$V = \exp\left[-(0.94np_2/l_c)^2\right].$$

This allows us to extrapolate to a grating interferometer with better-adapted parameters, e.g., a π-shifting first grating and a 2.4 μm analyzer grating period with the visibility around 45% at the 11th Talbot order, corresponding to 485 mm for the 19 keV design energy (see Ref. 9). Compared to our setup, this would provide a sensitivity gain of $\sqrt{2}$ from increased transmission, 2.9 from p_2, and 0.6 from d. The exact visibility cannot be calculated without knowing the coherence properties of the beamline, the motor stability, and the grating quality; however, our setup would be favored due to the smaller np_2 (i.e., more robust against transverse incoherence). The spatial resolution is limited to at least twice p_2, and thus, the optimized setup would allow for CNR gain from filtering. We predict that an optimized grating interferometer could reasonably achieve four times greater sensitivity. This image quality improvement over absorption is still far less than the $\Delta\delta/\Delta\beta$ ratio and should be weighed against the more complicated and time-consuming acquisition of XDGI.

TABLE II. Means and standard deviations of the measured index of refraction for each feature relative to paraffin. The values correspond to $(\Delta\delta \pm \sigma_\delta) \times 10^{-8}$ for DPC 20, $(\Delta\beta \pm \sigma_\beta) \times 10^{-11}$ for ABS 20, and $(\Delta\beta \pm \sigma_\beta) \times 10^{-10}$ for ABS 10.

	CNR	RCG	Paraffin	Molecular layer	White matter	Granular layer
DPC 20	17.2 ± 2.7	1.0	0 ± 0.22	3.62 ± 0.26	4.51 ± 0.23	5.06 ± 0.38
ABS 10 (filtered)	10.6 ± 1.2	1.6	0 ± 0.33	4.03 ± 0.40	4.80 ± 0.49	5.13 ± 0.71
ABS 10 (unfiltered)	2.2 ± 0.2	7.8	0 ± 1.54	3.89 ± 1.94	4.63 ± 2.23	4.96 ± 3.13
ABS 20 (filtered)	4.2 ± 0.3	4.1	0 ± 1.34	5.47 ± 1.42	6.29 ± 1.63	7.27 ± 1.85
ABS 20 (unfiltered)	0.3 ± 0.02	58.7	0 ± 18.97	5.46 ± 21.02	6.31 ± 22.04	7.26 ± 28.60

In conclusion, we report a quantitative measurement of the refractive index for a specimen of medical relevance. We show that a substantial part of the CNR gain from XDGI to absorption can be compensated by the loss in the spatial resolution from grating interferometry. We also show that when the photon energy is selected to optimize absorption measurements, the CNR gain from XDGI is substantially smaller. This plays an important role because it is technically easier to optimize the photon energy for an absorption measurement than for a grating interferometer. Our results indicate that for paraffin-embedded specimens, absorption tomography is a very attractive time-, cost-, and effort-effective approach. Depending on the specific application, these advantages can play a defining role, as in the case of time-critical biopsy evaluations or high-throughput animal experiments that require the processing of hundreds of samples. These results emphasize the complex relationship between CNR and the spatial resolution as well as the importance of considering the optimization procedures for each technique when comparing imaging modalities.

REFERENCES

[1] U. Bonse and M. Hart, Appl. Phys. Lett. **6**, 155 (1965).

[2] A. Momose, Jpn. J. Appl. Phys., Part 1 **44**, 6355 (2005).

[3] U. Bonse, Phys. J. **53**, 211 (1997).

[4] A. Momose, T. Takeda, Y. Itai, K. Hirano, and A. Yoneyama, Synchrotron Radiat. News **11**, 27 (1998).

[5] G. Schulz, T. Weitkamp, I. Zanette, F. Pfeiffer, F. Beckmann, C. David, S. Rutishauser, E. Reznikova, and B. Müller, J. R. Soc. Interface **7**, 1665 (2010).

[6] S. E. Hieber, C. Bikis, A. Khimchenko, G. Schweighauser, J. Hench, N. Chicherova, G. Schulz, and B. Müller, Sci. Rep. **6**, 32156 (2016).

[7] A. Khimchenko, C. Bikis, A. Pacureanu, S. E. Hieber, P. Thalmann, H. Deyhle, G. Schweighauser, J. Hench, S. Frank, M. Müller-Gerbl *et al.*, Adv. Sci. **5**, 1700694 (2018).

[8] J. Albers, S. Pacilé, M. A. Markus, M. Wiart, G. Vande Velde, G. Tromba, and C. Dullin, Mol. Imaging Biol. **20**, 732 (2018).

[9] I. Zanette, T. Weitkamp, G. Le Duc, and F. Pfeiffer, RSC Adv. **3**, 19816 (2013).

[10] M. Töpperwien, F. van der Meer, C. Stadelmann, and T. Salditt, Proc. Natl. Acad. Sci. U. S. A. **115**, 6940 (2018).

[11] A. Khimchenko, H. Deyhle, G. Schulz, G. Schweighauser, J. Hench, N. Chicherova, C. Bikis, S. E. Hieber, and B. Müller, NeuroImage **139**, 26 (2016).

[12] C. Bikis, P. Thalmann, L. Degrugillier, G. Schulz, B. Müller, D. F. Kalbermatten, S. Madduri, and S. E. Hieber, J. Neurosci. Methods **294**, 59 (2018).

[13] D. Paganin, *Coherent X-ray Optics* (Oxford University Press, 2006).

[14] T. Weitkamp, A. Diaz, C. David, F. Pfeiffer, M. Stampanoni, P. Cloetens, and E. Ziegler, Opt. Express **13**, 6296 (2005).

[15] F. Pfeiffer, O. Bunk, C. Kottler, and C. David, Nucl. Instrum. Methods Phys. Res. A **580**, 925 (2007).

[16] L. Grodzins, Nucl. Instrum. Methods Phys. Res. **206**, 541 (1983).

[17] P. Thurner, F. Beckmann, and B. Müller, Nucl. Instrum. Methods Phys. Res. B **225**, 599 (2004).

[18] A. Andronache, M. von Siebenthal, G. Szekely, and P. Cattin, Med. Image Anal. **12**, 3 (2008).

[19] F. Maes, A. Collignon, D. Vandermeulen, G. Marchal, and P. Suetens, IEEE Trans. Med. Imaging **16**, 187 (1997).

[20] P. Viola and W. M. Wells III, Int. J. Comput. Vision **24**, 137 (1997).

[21] A. K. Stalder, B. Ilgenstein, N. Chicherova, H. Deyhle, F. Beckmann, B. Müller, and S. E. Hieber, Int. J. Mater. Res. **105**, 679 (2014).

[22] G. Schulz, C. Waschkies, F. Pfeiffer, I. Zanette, T. Weitkamp, C. David, and B. Müller, Sci. Rep. **2**, 826 (2012).

[23] R. Raupach and T. G. Flohr, Phys. Med. Biol. **56**, 2219 (2011).

[24] K. J. Engel, D. Geller, T. Köhler, G. Martens, S. Schusser, G. Vogtmeier, and E. Rössl, Nucl. Instrum. Methods Phys. Res. A **648**, S202 (2011).

[25] D. Hahn, P. Thibault, M. Bech, M. Stockmar, S. Schleede, I. Zanette, A. Rack, T. Weitkamp, A. Sztrókay, T. Schlossbauer, F. Bamberg, M. Reiser, and F. Pfeiffer, Biomed. Opt. Express **3**, 1141 (2012).

[26] D. Paganin, S. C. Mayo, T. E. Gureyev, P. R. Miller, and S. W. Wilkins, J. Microsc. **206**, 33 (2002).

[27] T. Thuering and M. Stampanoni, Philos. Trans. R. Soc. A **372**, 20130027 (2014).

[28] T. Weitkamp, C. David, C. Kottler, O. Bunk, and F. Pfeiffer, *Developments in X-Ray Tomography V* (International Society for Optics and Photonics, 2006), Vol. 6318, p. 63180S.